Bull Volcanol (2014) 76:795
DOI 10.1007/s00445-014-0795-9

RESEARCH ARTICLE

The 2007–8 volcanic eruption on Jebel at Tair island (Red Sea) observed by satellite radar and optical images

Wenbin Xu · Sigurjón Jónsson

Received: 30 May 2013 / Accepted: 5 January 2014 / Published online: 31 January 2014

Abstract We use high-resolution optical images and Interferometric Synthetic Aperture Radar (InSAR) data to study the September 2007–January 2008 Jebel at Tair eruption. Comparison of pre- and post-eruption optical images reveals several fresh ground fissures, a new scoria cone near the summit, and that 5.9±0.1 km^2 of new lava covered about half of the island. Decorrelation in the InSAR images indicates that lava flowed both to the western and to the northeastern part of the island after the start of the eruption, while later lavas were mainly deposited near the summit and onto the north flank of the volcano. From the InSAR data, we also estimate that the average thickness of the lava flows is 3.8 m, resulting in a bulk volume of around 2.2×10^7 m^3. We observe no volcano-wide pre- or post-eruption uplift, which suggests that the magma source may be deep. The co-eruption interferograms, on the other hand, reveal local and rather complex deformation. We use these observations to constrain a tensile dislocation model that represents the dike intrusion that fed the eruption. The model results show that the orientation of the dike is perpendicular to the Red Sea rift, implying that the local stresses within the volcanic edifice are decoupled from the regional stress field.

Keywords Red sea · InSAR · High-resolution optical satellite imagery · Volcanology

Editorial responsibility: M.R. Patrick

Electronic supplementary material The online version of this article (doi:10.1007/s00445-014-0795-9) contains supplementary material, which is available to authorized users.

W. Xu (✉) · S. Jónsson
King Abdullah University of Science and Technology (KAUST), Thuwal, Saudi Arabia
e-mail: wenbin.xu@kaust.edu.sa

Introduction

The Red Sea is a divergent plate boundary between the African and the Arabian plates with an opening rate that increases from 7 mm/year in the north to 16 mm/year in the south (ArRajehi et al. 2010). In the southern Red Sea, the rift boundary splits into two branches (Fig. 1a), with one branch following the Red Sea with decaying opening rate to the southeast and the other branch lying along the Danakil depression and meeting up with the East African rift and the Aden ridge (McClusky et al. 2010). The Jebel at Tair island is an oval-shaped stratovolcano, located in the south-central Red Sea between Yemen and Eritrea. This small island is only ~4 km long, covering an area of about 11.4 km^2, and its highest peak is 258 m above sea level (Fig. 1b). The surface of Jebel at Tair is covered by tholeiitic basaltic lava flows and is cut by numerous open radial fissures (Gass et al. 1973). The most recent volcanic eruptions on the island (before 2007) were in 1833, 1863, and in 1883, and possibly during the eighteenth century (Smithsonian Institution 2007). The island has been uninhabited, apart from a small Yemeni military outpost.

In the afternoon of 30 September 2007, an energetic fissure eruption started on Tair island, depositing lavas to the NE and W of the summit and destroying the military outpost, resulting in several casualties (Smithsonian Institution 2007). Visual inspection made by Yemeni scientists from a helicopter on 1 October 2007 showed lava fountaining from a short fissure extending from the summit area and down to the northeastern flank of the volcano (Jamal Sholan, personal communication, 2012). Steam plumes were seen rising from fissures on the west flank but no lava fountaining in the west was observed, though fresh lava flows were seen in this area extending down to the shore. A new summit scoria cone had formed above the northeastern fissure on 21 October 2007, when a field trip was carried out to the island, and at that time lava mainly came

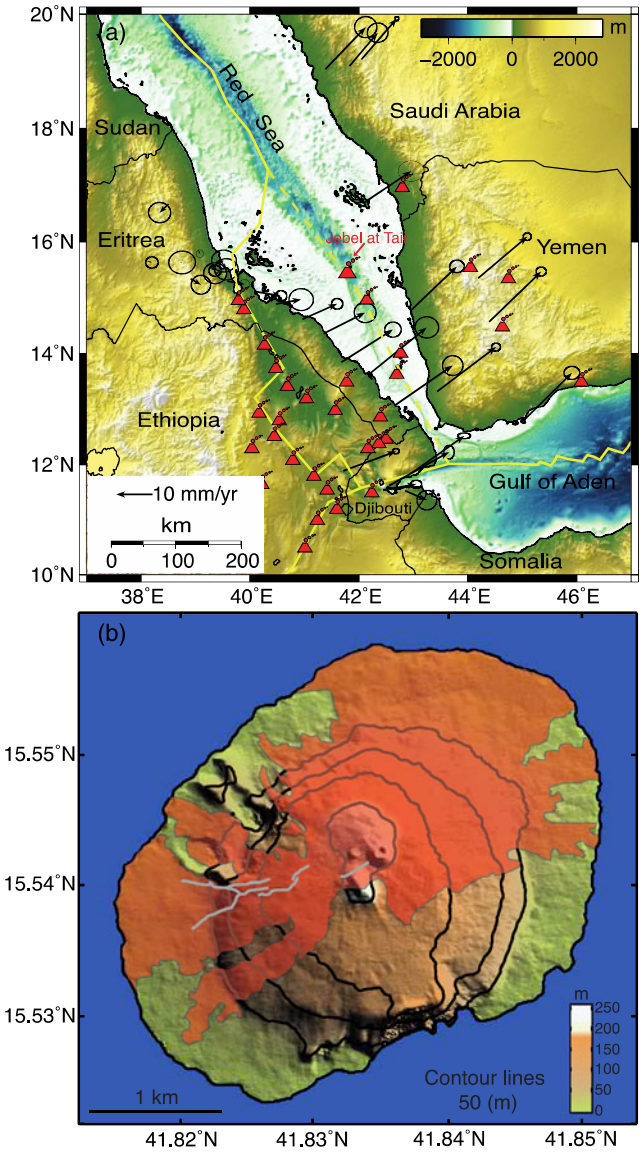

Fig. 1 **a** Topography and bathymetry of southcentral Red Sea (http://topex.ucsd.edu/WWW_html/srtm30_plus.html), where the Jebel at Tair volcano is located. *Red symbols* show locations of volcanoes (Siebert et al. 2010), *yellow lines* mark plate boundaries in the region (Bird 2003), *black arrows* show GPS velocities with 95 % confidence ellipses in a Eurasia-fixed reference frame (ArRajehi et al. 2010). **b** TanDEM-X DEM shaded relief topography of Jebel at Tair island with 50 m elevation contour lines. The coverage of the new lavas is shown in *red* and several new ground fissures are in *gray*

from that scoria cone (Jamal Sholan, personal communication, 2012). No further direct field observations were made of the volcanic eruption by Yemeni scientists and it has not been clear how long the eruption lasted. However, a series of SEVERI (Spinning Enhanced Visible and InfraRed Imager) images show that a thermal anomaly observed from the onset of the eruption disappears around 15 January 2008 (±1 day) (Talfan Barnie, personal communication, 2012), which indicates that the total duration of 2007–2008 Jebel at Tair volcanic eruption was 107 days.

Clarisse et al. (2008) analyzed volcanic SO_2 with an Infrared Atmospheric Sounding Interferometer (IASI) and tracked the plume of the Jebel at Tair eruption for the first 12 days. Shibata and Kouketsu (2008) studied the volcanic clouds from the Tair eruption using both a ground-based Lidar in Nagoya, Japan and a space-borne aerosol Lidar onboard the CALIPSO satellite and found the clouds to be nondepolarized and not composed of ice particles and that they were transported from the troposphere to the stratosphere. Temperature profiles also indicate that the eruption cloud penetrated the tropopause and reached 16 km altitude (Eckhardt et al. 2008).

The Jebel at Tair volcanic eruption occurred in a remote and mostly uninhabited area where no seismometers or conventional geodetic instruments have been installed to monitor volcanic and earthquake activity. Earthquakes located by regional networks provide limited information, although they show increased seismicity near the island as early as 21 September 2007 (International Seismological Centre, ISC). At least four M_L>4 earthquakes occurred in the afternoon of 30 September, which probably coincided with the dike propagating to the surface. Given the lack of local instrument recordings and direct observations of the Tair eruption, remotely sensed data from satellites provide key information to understand and explain the course of events during the eruption and in the subsequent months.

In this study, we use high-resolution optical images and Interferometric Synthetic Aperture Radar (InSAR) data from satellites to study the 2007–2008 eruption. Commercially available optical satellite images have resolution as good as 50 cm and can provide important details about the surface change occurring in volcanic eruptions and other natural disasters. InSAR has proven to be a powerful tool for mapping crustal deformation with a centimeter to millimeter accuracy and at a high spatial resolution (Massonnet and Feigl 1998). We start by describing the high-resolution optical images and then the available InSAR data and the data processing. We document how the lava progressed during the eruption based on radar coherence time series maps, and generate pre- and post-eruption digital elevation models (DEMs) to estimate the subaerial volume of the lava flows. We also use the InSAR data to model the dike that fed the eruption, applying constraints from the optical images.

High-resolution satellite optical images

High-resolution satellite optical images acquired before and after the eruption provide detailed information about the surface changes on the island caused by the eruption. They help to understand the eruption activity, to find where ground

fissures opened, where new lava was deposited, and how the coastline changed.

We ordered three high-resolution cloud-free satellite images, one from before and two from after the eruption (Table 1). The first image was acquired by the Quickbird satellite about 3 months before the onset of the eruption on 6 July 2007 and it has 60 cm pixel resolution (Fig. 2a). The post-eruption images were acquired by the WorldView-1 satellite on 22 December 2008 (not shown) and the WorldView-2 satellite on 22 October 2011 (Fig. 2b) and these images have 50 cm pixel resolution. The co-eruptive changes can be clearly seen in both post-eruption images, but the 2011 image is of better quality and we therefore focus our co-eruption surface-change analysis on that image.

The pre-eruption Quickbird image shows that the island was covered by multiple old lava flows before the 2007 eruption began (Fig. 2a). Several radially distributed open fissures can be distinguished in the lava flows and two summit cones are visible (Fig. 3a).These cones can also be identified in the Tandem-X DEM (Fig. 1b). Older erosional sea cliffs are exposed on the southeastern shore of the island (Fig. 2), and these cliffs probably existed all around island, but were later mostly covered by lava flows (Gass et al. 1973). In addition to these natural features, several car tracks and buildings can be seen on the island in the pre-eruption image.

The post-eruption WorldView-2 image shows, when compared to the pre-eruption image, that about half of the island is covered by new lava flows, which appear black and gray–yellowish in color (Fig. 2b). The lava seems to have flowed mainly to the NE, N, and W from the summit of the volcano and all the way to the Red Sea coastline. Many of the buildings and most of the car tracks were buried by the lava flows.

The perimeter of the new lava flow is ~26.5 km and the area is 5.9 km^2, as mapped from this high-resolution optical satellite image. We were able to detect the flow edges with a precision of about 5 m (10× the spatial resolution of the WorldView-2 image), so we estimate the uncertainty of flow area determination to be ±0.1 km^2. The lava flowed to the sea both in the west and in the northeast, causing changes to the shoreline (Fig. 2b), enlarging the area of the island by

Table 1 Information about the SAR datasets and the high-resolution optical images

Satellite	Orbit	Track	Frame	Acq. date (month/date/year)	Perp. baseline (m)
ALOS	4,606	596	290	12/05/2006	142.2
	7,290	596	290	06/07/2007	−597.6
	7,961	596	290	07/23/2007	−225.1
	8,632	*596*	*290*	*09/07/2007*	*0*
	9,303	*596*	*290*	*10/23/2007*	*50*
	9,974	596	290	12/08/2007	82.2
	10,645	596	290	01/23/2008	215
	11,316	596	290	03/09/2008	462.1
	12,658	596	290	06/09/2008	947.4
	14,000	596	290	09/09/2008	−1,751.2
	15,342	596	290	12/10/2008	−1,212.4
	18,026	596	290	06/12/2009	−1,032.2
	18,697	596	290	07/28/2009	−1,119
	19,368	596	290	09/12/2009	−814.8
	20,039	596	290	10/28/2009	−540.3
	20,710	596	290	12/13/2009	−475.9
	22,723	596	290	04/30/2010	56.5
ENVISAT	*19,871*	*278*	*5425*	*12/18/2005*	*0*
	29,390	*278*	*5582*	*10/14/2007*	*−45*
ERS-2	*52,236*	*278*	*6576*	*04/17/2005*	*0*
	70,773	*278*	*6579*	*11/02/2008*	*105*
Tandem-X	*130*	–	–	*11/15/2011*	*−201.2*
	130	–	–	*12/26/2012*	*283.8*
Quickbird	–	–	–	*07/06/2007*	–
WorldView-1	–	–	–	12/22/2008	–
WorldView-2	–	–	–	*10/22/2011*	–

Note that TanDEM-X data, co-eruption interferograms, and optical images shown in italics are discussed in the text

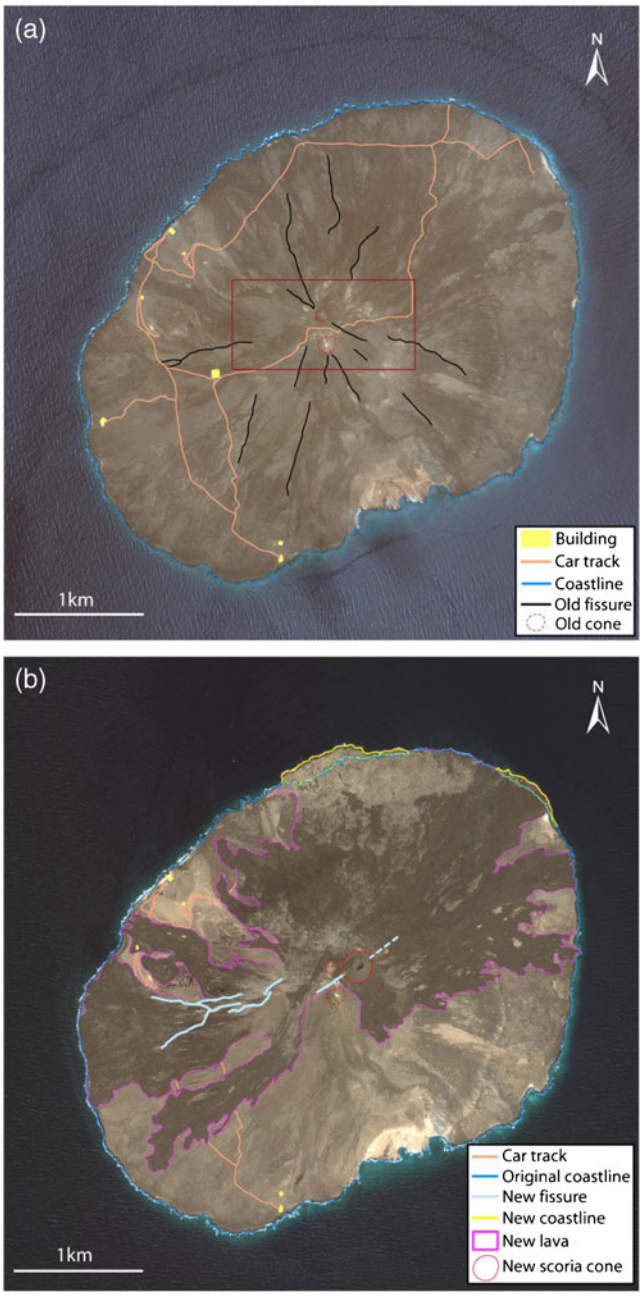

Fig. 2 High-resolution optical satellite images of Jebel at Tair volcano from before and after the 2007–2008 eruption. **a** The pre-eruption image was taken on 6 July 2007 (60 cm spatial resolution), showing that the small island was covered by old lava flows and radially distributed ground fissures. *Red rectangle* marks the area covered in Fig. 3. **b** The post-eruption image is from 22 October 2011 (50 cm resolution) and it shows the new lava flows (*pink*), a new scoria cone (*red*), several new ground fissures (*light blue*), possible buried new fissure (*dashed light blue*), and changes to the coastline (*yellow*) in the north

0.13 km^2. The new scoria cone seen in the field on 21 October is clearly visible in the image near the summit and it has a base diameter of ~0.25 km. We are not sure when it started to form, but an Envisat SAR amplitude image shows that it was already there on 14 October 2007. In addition, a Terra ASTER image from 8 October exhibits a strong point-like thermal anomaly at this location, indicating that the eruption had already focused on a single summit vent by that day (Smithsonian Institution 2007).

Several new eruptive fissures are seen in the post-eruption image (Fig. 3b). They were only active during the initial phase of the eruption, producing the lava that extends down to the shore in the west, north, and the northeast. One of the fissures lies right beneath the new scoria cone and extends ~0.25 km to the southwest of the cone with a N59°E orientation. It also extended several hundred meters down the flank to the northeast, as was seen during the visual inspection made from air on 1 October (Jamal Sholan, personal communication, 2012), but most of it was subsequently covered by lava flows from the new cone (Fig. 3b). Several small ground fissures can also be seen ~0.6–1.6 km west-southwest of the scoria cone (Fig. 2b). They are slightly offset to the north and have a somewhat different strike of ~N60°E–N90°E, when compared with the summit fissure. The total length of these fissures on the west flank is ~1.1 km. These eruptive fissures suggest that the eruption was fed by dikes with similar orientations at shallow depths.

Evolution of the lava flow

Mapping the extent and evolution of lava flows is critical to volcano monitoring and valuable for understanding lava flow dynamics. This type of mapping has in the past been primarily based on field observations, e.g., from handheld GPS measurements or on airborne surveys (Poland 2007), but in recent years decorrelation in InSAR images has increasingly been used for this task (e.g., Dietterich et al. 2012). Here, we generate multiple interferograms from 17 SAR images acquired between 5 December 2006 and 30 April 2010 by the ALOS satellite (L band, 23.6 cm wavelength) and use the interferometric coherence to map the evolution of the lava during the 2007–2008 Tair eruption (Table 1). Radar coherence in an interferogram is a manifestation of the similarity of the surface-scattering properties between the two radar acquisitions that were used to form that interferogram. In areas of no change between InSAR images, the coherence of the generated interferograms is generally high, even for multiyear interferograms. However, when new lava is deposited, the surface scattering properties change completely, resulting in total decorrelation of the interferometric signal in the area covered by the new lava. Based on the decorrelated area in the InSAR data, we map the extent of new lava with time during the eruption (Dietterich et al. 2012). However, rapid lava cooling, resulting in thermal contraction and physical compaction, can also cause interferometric decorrelation, which can be difficult to discriminate from decorrelation caused by new lava emplacement in the coherence maps.

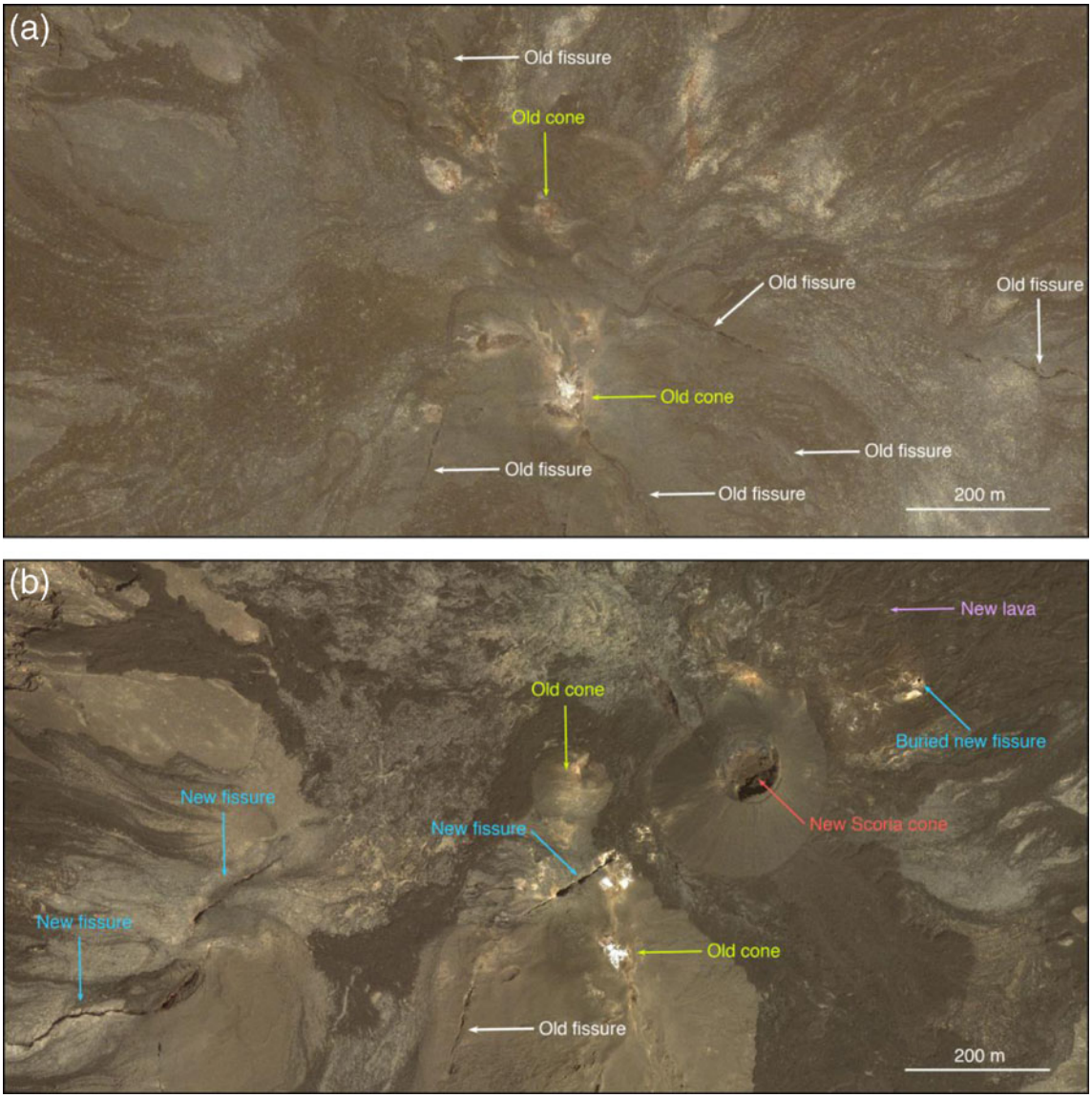

Fig. 3 The details in the summit area (see coverage in Fig. 2a) before and after the eruption. **a** The pre-eruption image shows several old fissures and two old cones, while the post-eruption **b** image shows clearly the new scoria cone and lava flows, as well as several new fissures, one located beneath the scoria cone and extending into the saddle between the two old cones

In the radar data processing, we followed a standard two-pass approach, with effects of the topography removed by using the SRTM DEM (Farr et al. 2007). The raw radar data were processed to SAR images and interferograms using the GAMMA software (Werner et al. 2000). We spatially averaged (multilooked) the interferograms using a 1×3 pixel window to reduce noise, then filtered them with an adaptive filtering algorithm (Goldstein and Werner 1998), and unwrapped the interferograms using a statistical minimum cost-flow unwrapping algorithm (Chen and Zebker 2001). The unwrapped interferograms together with their corresponding decorrelation maps were then finally projected to geographic coordinates.

The coherence maps (Fig. 4) show the evolution of the lava flows during the eruption and confirm that the eruptive activity was most vigorous during the first phase. The time resolution of this method is limited due to the long repeat time of the ALOS satellite (46 days), which provides only three possible windows to study the evolution of the lava during the eruption. Decorrelation in an interferogram that spans the first 23 days of the eruption shows that lavas were deposited to the west, north, and northeast, reaching the Red Sea (Fig. 4a). In fact, most of this lava was likely produced in the first 2 days as by 1 October the lava had already reached the shoreline, according to the aerial inspection mentioned above. The estimated subaerial area of the lava deposited in the first 23 days

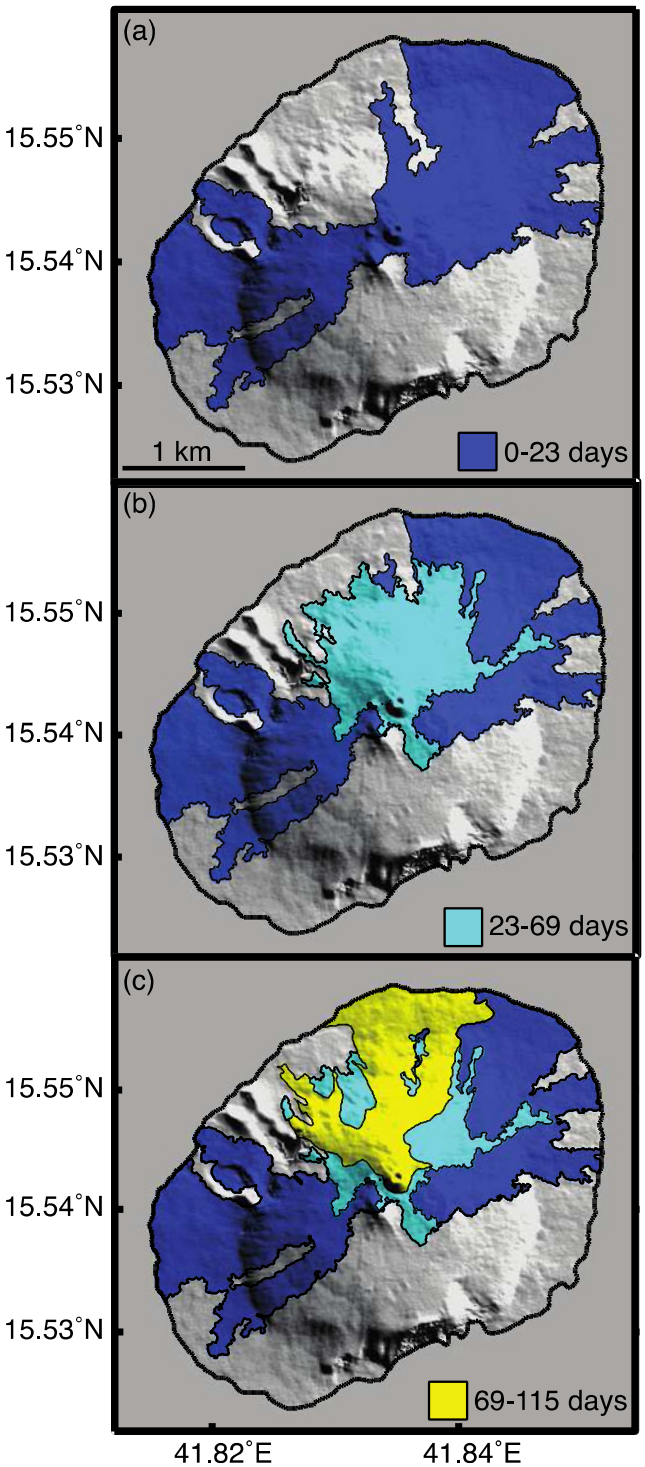

Fig. 4 Evolution of the lava flow during the Jebel at Tair eruption. The areas covered by new lava during the first 23 days, between days 23 and 69 after the start of the eruption, and between days 69 and 115 are shown in *blue*, *light blue*, and *yellow*, respectively

is about 4.9 km^2 (see Table 2), which is a majority of the eventual 5.9±0.1 km^2 total subaerial area of the 2007–2008 lava. The lavas produced during the two subsequent time periods primarily flowed to the north of the summit, partly

Table 2 Information on the evolution of lava flow after the onset of the 2007–2008 Jebel at Tair volcanic eruption

Days	Dates	Area (km^2)	Reached the sea
0–23	30 Sep 2007–23 Oct 2007	4.9	Yes
23–69	23 Oct 2007–8 Dec 2007	1.7	No
69–115	8 Dec 2007–23 Jan 2008	1.4	Yes
0–115	30 Sep 2007–23 Jan 2008	5.9	Yes

Note that summing up the area values from the individual time periods exceeds the total area, as the subsequent lavas partly cover the earlier lavas

covering the earlier lava from the first period as well as covering new ground. The area of the lava produced during the second phase of the eruption (23–69 days after the start of the eruption) is smaller than during the first phase or about 1.7 km^2, and it did not reach the Red Sea (Fig. 4b). During the third period (69–115 days after the start), lava continued to flow to the north, reaching the coast again, with a subaerial flow area of about 1.4 km^2 (Fig. 4c).

A time series of satellite thermal images from MODIS and SEVIRI instruments suggests that the eruption ended on 15 January 2008 (±1 day), as discussed above (Talfan Barnie, personal communication, 2012). However, satellite data used in the Hawai'i Institute of Geophysics and Planetology (HIGP) Thermal Alerts System show intermittent thermal anomalies after 15 January, i.e., until mid-May 2008 (Smithsonian Institution 2008). The ALOS data do not provide precise information about when the eruption ended, due to the long 46-day repeat time. Post-eruption decorrelation maps, formed using ALOS data from 23 January to 9 June 2008, show reduced coherence of a ~0.8 km^2 area near the summit. This reduction of coherence is probably due to rapid lava flow cooling and physical compaction, rather than new lava, as the coherence is not completely lost. We therefore think that the eruption did not continue until May 2008, but ended on 15 January 2008 (±1 day) and that the intermittent thermal anomalies after 15 January may have been due to low-level residual activity around hot open, degassing vent(s).

Lava flow volume

We also used multiple ALOS interferograms and TanDEM-X data (Krieger et al. 2007) to derive pre- and post-eruption DEMs, respectively, to estimate the total volume of the 2007–2008 Jebel at Tair lava flows (Table 1). The pre-eruption and post-eruption DEMs were generated from interferograms with different perpendicular baselines ranging from 142 to 740 m, corresponding to heights of ambiguity between 18 and 452 m. The height of ambiguity is defined as the height difference that generates a full interferometric phase cycle

(i.e., 2π) after interferogram flattening and is inversely proportional to the perpendicular baseline (Massonnet and Feigl 1998). The interferogram with a longer baseline has a smaller height of ambiguity and is therefore more sensitive to topography. In order to improve the accuracy of the final DEMs, we first derived height values from N interferograms and then calculated a weighted average based on the interferogram coherence and perpendicular baseline (Eq. 1), as proposed by Lu et al. (2003):

$$h = \frac{\sum_i^N h_i C_i B_i^2}{\sum_i^N C_i B_i^2} \quad (1)$$

where h_i is the height value derived from interferogram i, C_i is the coherence and B_i is the perpendicular baseline of that interferogram. When the pre-eruption DEM is subtracted from the SRTM DEM, the resulting residual DEM shows random noise, a phase ramp, and detailed terrain structure. We first low-pass filtered the residual DEM to reduce the noise level, then fit a polynomial function to remove the phase ramp which mainly includes atmospheric effects and orbit errors, leaving only the detailed terrain information, which we added to SRTM DEM to form the final pre-eruption DEM (Rowland et al. 2003; Wadge et al. 2006).

The difference between the pre- and post-eruption DEMs reveals the topographic height change caused by the eruption, which is primarily due to the deposition of lavas and the formation of the new summit scoria cone. A histogram of the refined height differences in areas with no new lava flows has a symmetrical distribution that peaks at zero and standard deviation of 1.9 m (Fig. 5), which indicates that the DEMs are well aligned. For the standard deviation calculation, we excluded the area near the southern cliff where radar geometrical distortions are severe. An alternative way to estimate lava thickness is simultaneously inverting the interferometric phase for topographic change and displacement (Ebmeier et al. 2012).

Examining the derived height change map (Fig. 5), we find significant positive elevation changes in and close to the new scoria cone with a maximum value of ~60 m and a notable positive height difference of about 20–40 m on the northern flank. We estimate the average subaerial thickness of the 2007–2008 volcanic products to be about 3.8 m (Table 3). Visual inspections made in the field indicate that the average lava thickness near the coast is similar or about 3 m (Jamal Sholan, personal communication, 2012). We estimate the bulk flow volume to be $2.2\pm1.1\times10^7$ m^3 by integrating the height changes within the area of the new lava. This estimated volume only includes the amount of lava that appears above sea level. The majority of 2007–2008 flows are ‘a’ā (Jamal Sholan, personal communication, 2012), and therefore the dense-rock equivalent (DRE) volume is smaller, here estimated $\sim1.7\pm0.8\times10^7$ m^3, assuming 25 % vesicularity.

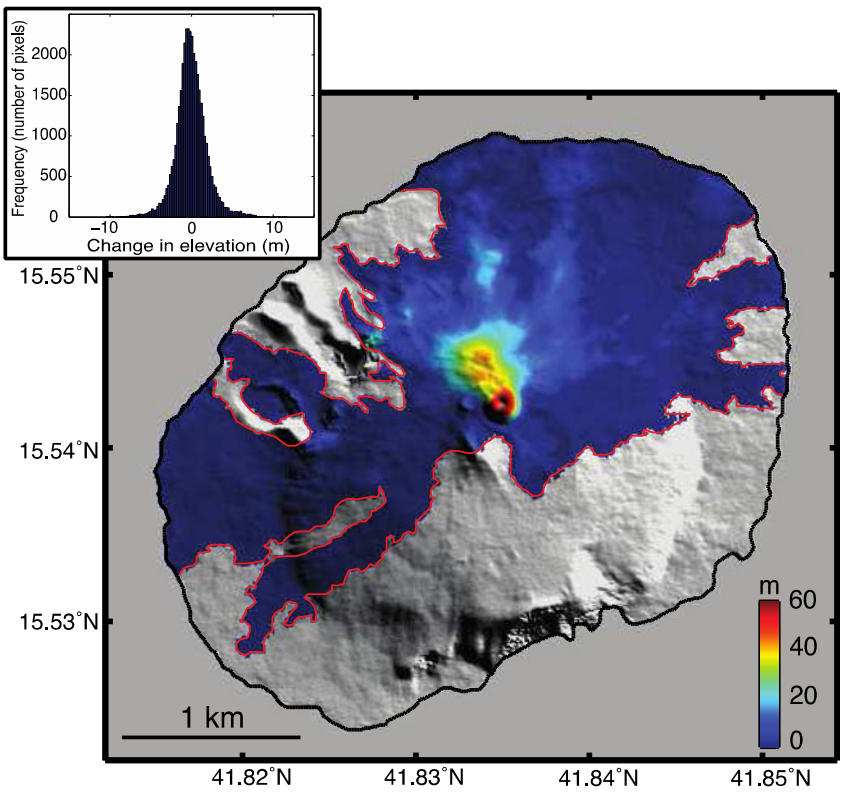

Fig. 5 Elevation change between the pre-eruption DEM, generated from ALOS interferograms, and the TanDEM-X post-eruption DEM. The *inset* shows a histogram of the DEM differences (standard deviation, 1.9 m) for areas not covered by the new lava flow

Table 3 Information on the Jebel at Tair lava flow volume, determined from pre- and post-eruption DEM height differences

Parameter	Value	Method
Subaerial area	5.9±0.1 km^2	Optical image and InSAR decorrelation
Average subaerial thickness	3.8±1.9 m	DEM difference
Max. subaerial thickness	~60 m	DEM difference
Subaerial DRE volume	~1.7±0.8×10^7 m^3	DEM difference, assuming 25 % vesicularity
Dike DRE volume	~5.0×10^6 m^3	Dike model

Observed deformation with InSAR

Interferograms that span the start of the eruption show a significant amount of ground deformation that likely occurred during the propagation of the magmatic dike to the surface. In contrast, we found no clear volcano-wide deformation in the pre-eruption interferograms we generated (ERS/Envisat data November 2003–December 2005, and ALOS data December 2006–September 2007) or in post-eruption interferograms (ERS/Envisat data July 2008–November 2009 and ALOS data January 2008–April 2010), which may indicate that the source of the magma is deep. Three interferograms provide the most valuable information: an ALOS interferogram spanning the first 23 days of the eruption (7 September–23 October 2007), an Envisat interferogram covering the time from 2 years before until 2 weeks after the start of the eruption (18 December 2005–14 October 2007), and an ERS interferogram that spans the entire eruption (Fig. 6a–c, Table 1). Both the Envisat and ERS data are C band (5.6 cm wavelength), have mean incidence angles of 23°, and were acquired from descending orbits (westward looking). They therefore show more or less the same line-of-sight (LOS) deformation and are more sensitive to vertical ground deformation than to horizontal displacements. The coverage of the Envisat data is better, owing to the larger extent of the new lava in the ERS interferogram. The L-band (23.6 cm wavelength) ALOS data, on the other hand, have a mean incidence angle of 38° and were acquired from ascending orbits (eastward looking). They therefore provide another perspective of the surface deformation and are sensitive to both horizontal and vertical deformation of the land surface.

All three interferograms exhibit multiple fringes of deformation on the northwestern and southeastern part of the island (Fig. 6a–c), but decorrelated areas correspond to the coverage of new lava flows. The ALOS interferogram has about one fringe (11.8 cm) in the northern part of the island and also south of the summit, as well as several fringes along some edges of the new lava flow (Fig. 6a). The fringe patterns in the Envisat and ERS interferograms (Fig. 6b–c) are quite complicated but consistent, suggesting that the deformation occurred during the onset of the eruption. The similarity of these two datasets also shows that atmospheric effects and orbital errors are negligible. The broad fringes in the southwest and southeast indicate that the co-eruption ground deformation probably extended significantly beyond the coast of the island. We unwrapped the ALOS and Envisat interferograms to quantify the magnitude of the LOS displacements in these datasets (Fig. 6d–e). The magnitude of the LOS displacements in the ALOS data is about 15 cm northwest of the summit and more than −35 cm along the edges of lava flows (Fig. 6d). The unwrapped Envisat interferogram (Fig. 6e) shows about 30 cm LOS displacement near the coast in the northeast, which is not seen in the ALOS data. Generally, the magnitude of displacement on the northern part of the island is smaller than that of the southern part.

In addition to the InSAR data, we calculated pixel offsets in the azimuth direction by cross-correlating 64×64 pixel subimages within the two ALOS amplitude images. This azimuth offset (AZO) measurement is only sensitive to horizontal displacements along the satellite azimuth direction, which is approximately perpendicular to the eruptive fissures. The AZO results show clear surface displacements with a peak-to-peak amplitude of ~1.2 m across the summit of the island (Fig. 6f). At the north of the summit, the ground moved to the north and the southern part of the island moved to the south, indicating that the intruding dike pushed the summit flanks of the mountain in opposite directions away from the dike.

Deformation modeling

The orientation of the eruptive fissures on Jebel at Tair shows that a southwest–northeast trending dike fed the eruption. To model the dike intrusion, we use rectangular dislocations in a homogeneous, isotropic, elastic half-space without considering the topography (Okada 1985) and compare the resulting model displacements with the main characteristics of the observed surface deformation associated with the eruption. Both the ALOS and the Envisat interferograms (Fig. 6d–e), as well as the AZO results (Fig. 6f), were used to constrain the source model parameters of the dike intrusion.

Estimating the size, location, dip, strike, and opening of multiple dike dislocations without any constraints can be both computationally challenging and unstable, e.g., leading to dissimilar solutions in independent model optimizations. We therefore used information from the post-eruption optical satellite image and from field observations to fix several parameters of the dike model. We first let the model dike

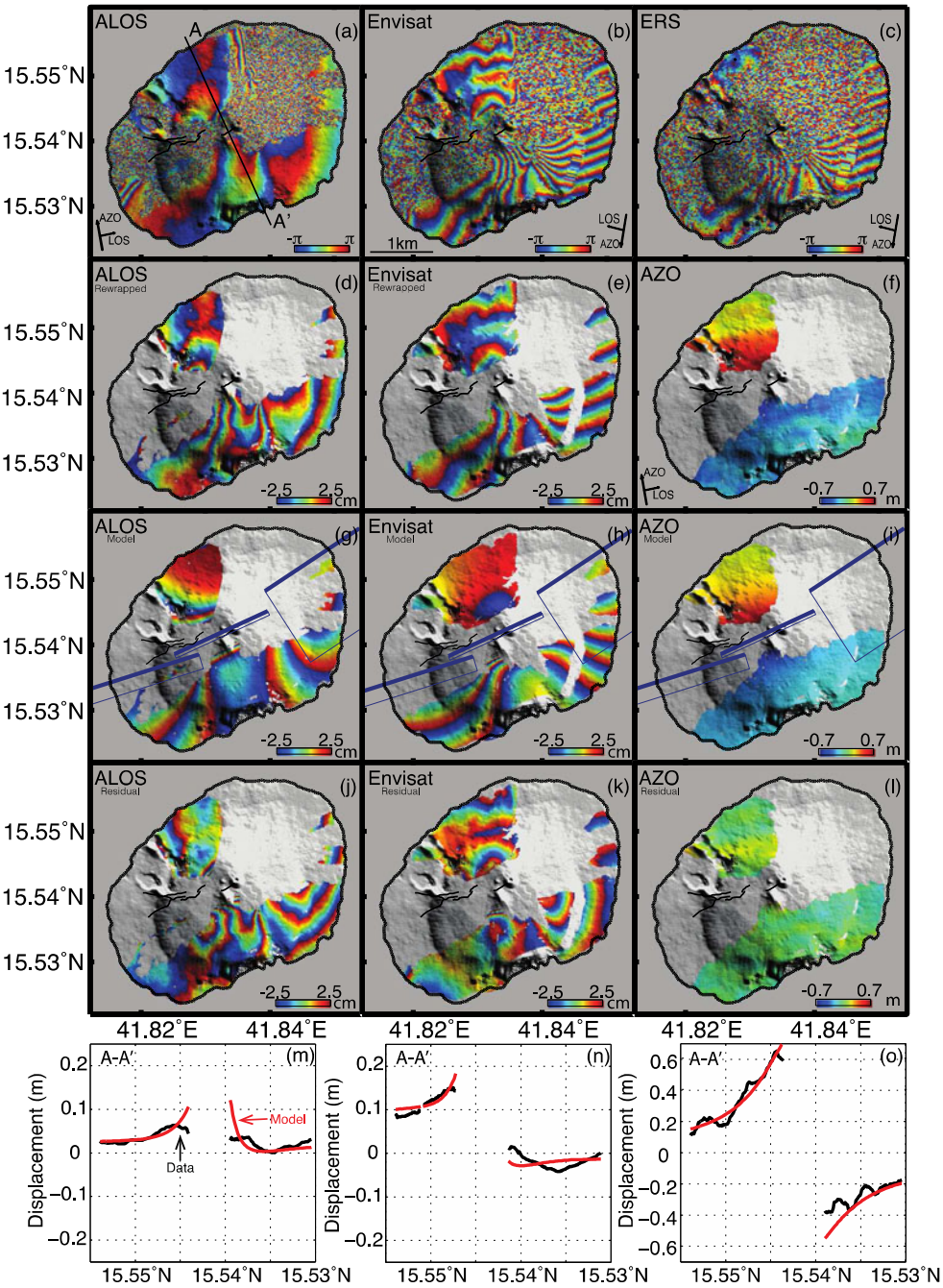

Fig. 6 **a** Filtered L-band co-eruption ALOS interferogram acquired from an ascending orbit with each color cycle corresponding to 11.8 cm of line-of-sight (LOS) displacement away from (*blue–green–yellow–red*) or toward (*red–yellow–green–blue*) the satellite. *Arrows* indicate the horizontal projection of the radar look direction (LOS) and the radar azimuth direction (AZO). New ground fissures are shown as *black bold lines*. **b**, **c** Filtered co-eruption Envisat and ERS interferograms from a descending orbit, with each color cycle corresponding to 2.8 cm (C band) displacement in LOS. **d** and **e** The ALOS and Envisat interferograms, rewrapped (after unwrapping) at 5 cm per fringe. **f** Azimuth offsets of ALOS radar amplitude images (AZO). **g–i** The model predictions that correspond to **d–f**. *Blue lines* the surface projections of the three model dikes, with *thicker lines* marking dike upper edges (parameters listed in Table 4). **j–l** Residuals between the observations and the model predictions, **m–o** the data (*black*) and model prediction (*red*) along profile *A–A′* for the ALOS, Envisat and AZO data sets, respectively

coincide with the mapped ground fissures by fixing its location, length, and strike. We extended the length of this summit dike by 0.3 km to the northeast in accord with the field observations ("Introduction" and "High-resolution satellite optical images" sections). The InSAR observations show that the deformation extends to the east and southwest of the summit fissure and we therefore added flank dike extensions to the summit dike (Fig. 7), whose parameters we allowed to vary in the parameter estimation. The data were uniformly subsampled (Pritchard et al. 2002) and we masked out the large local signals in the ALOS interferogram (Fig. 6a), because they are not directly related to the diking process but likely to loading of lava. We used a Monte Carlo-type simulated annealing algorithm (Cervelli et al. 2001) to find the optimal dike geometry and the uniform opening. In addition, we allowed for constant dataset shifts (ambiguities) in the modeling, as the entire island was deforming and therefore no obvious zero displacement reference point exists. With this modeling setup, the number of degrees of freedom is 21.

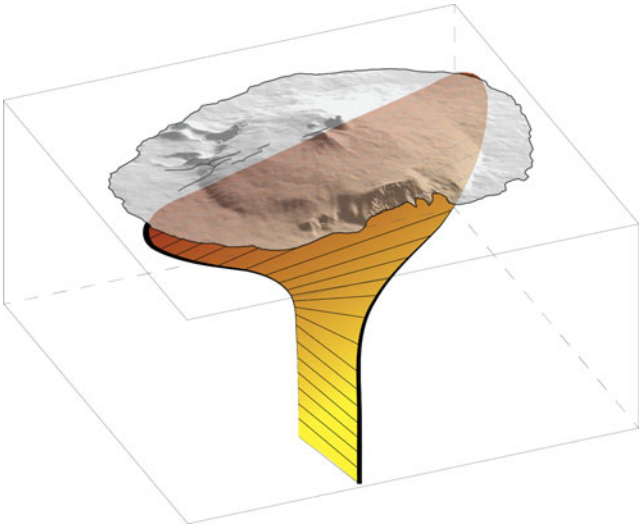

Fig. 7 Three-dimensional representation of the model dikes based on the results of this study

The predicted surface deformation of this combination of three dislocations representing one long dike can explain the most prominent deformation signals well, i.e., the northwest–southeast extension seen in the AZO data (Fig. 6i) and the complex deformation pattern seen in the Envisat data (Fig. 6h). This is confirmed by the low residual Envisat RMS value of ~2.2 cm and the rather flat AZO residual (RMS value of 6.2 cm, Fig. 6k–l). The RMS value to the ALOS data is 3 cm, leaving some unmodeled deformation in the southeastern part of the island (Fig. 6m–o). The model parameter estimation yielded a near vertical and 2 m thick summit dike with a length of 1.5 km (Table 4). The attached flank dike extensions to the northeast and southwest bring the total length of the shallow dikes to 5.9 km. The extensions have slightly different orientations and are thinner than the summit dike and their bottoms are deeper than the central summit dike (Table 4). The northeastern flank dike extension was made to dip to the southeast (Table 4) to fit the strong deformation seen in the Envisat interferogram on the eastern part of the island. The bulk volume of the multidike dike model is $\sim 5.0 \times 10^6$ m^3 or around 30 % of the derived lava volume. We also explored a four-dike model that includes a deeper dike that is parallel to the Red Sea rift, but this model does not significantly improve the fit to the data (see Electronic supplementary material for details).

The entire eruptive fissure was active for only the first several hours of the eruption, as by 1 October lava flowed only from a short summit fissure (Jamal Sholan, personal communication, 2012). Assuming that the length of eruptive fissure steadily decreased from 1.5 km on 30 September (3 pm) to 0.3 km on 1 October (10 am), we estimate the effusion rate using:

$$E_{\text{mean}} = \frac{w^3 l\left(\frac{\mathrm{dp}}{\mathrm{dz}} - g\rho\right)}{12\eta} \tag{2}$$

where $\frac{\mathrm{dp}}{\mathrm{dz}}$ is the lithostatic pressure gradient, w and l the average thickness and length of the eruptive dike, g the gravitational acceleration, and ρ and η are the density and viscosity of the magma, respectively (Rowland et al. 2003). If we use w=1.1 m, ρ=2,600 kg/m^3 and η=300 Pa s, and take the value of $\frac{\mathrm{dp}}{\mathrm{dz}}$ to be 27 kPa/m, then the calculated effusion rate E_{mean} decreased from ~843 m^3/s at the onset of the eruption to ~168.6 m^3/s on 1 October. Integrating the lava effusion rate E_{mean} for the time span mentioned above we find lava volume of $\sim 3.5 \times 10^7$ m^3, which is larger than the estimated total lava volume ("Lava flow volume" section). This discrepancy suggests that an amount of lava may have entered the sea, some parameters in Eq. 2 are different (e.g., the pressure gradient), or this simple approach over-estimates the volume due to some incorrect assumptions.

Post-emplacement lava flow deformation

Lava flows continue to deform after they have been emplaced (e.g., Stevens et al. 2001; Lu et al. 2005), but the deformation mechanism is not well understood. Phase decorrelation on young 'a'ā lava flows results from movement of surface blocks (scatterers), rapid compaction of the lava flows and surface clast repacking (Ebmeier et al. 2010), often preventing interferometric analysis of the lava flow movement during the first weeks after emplacement. In order to minimize this type

Table 4 Information about the dike-model parameters from modeling the data for the co-eruption time period

	Length (km)	Width (km)	Depth (km)	Dip (°SE)	Strike (°NE)	Latitude (°N)	Longitude (°E)	Opening (m)
Dike I	2.28	1.99	0.1	83	73	15.535	41.819	0.6
Dike II	1.5	0.17	0	67	66	15.542	41.833	2.0
Dike III	1.89	2.98	0	62	57	15.553	41.847	0.6

Note that the depth is the top depth of dikes

of decorrelation, we use ten consecutive ALOS interferograms to study the post-emplacement lava flow deformation after 23 January 2008 using a chain stacking approach (Biggs et al. 2007; Xu et al. 2012). In this method, all the interferograms are added up to retrieve the accumulated deformation, which eliminates atmospheric effects and orbital errors in the middle of the chain of images, leaving only the error contributions from the first and last image.

The main post-emplacement lava flow subsidence is found north of the summit cone (Fig. 8a) with maximum LOS displacement of ~−1.1 m, corresponding to a mean subsidence rate of up to −0.5 m/year. Three "branches" of subsidence extend down the north flank and correlate well with areas of greatest lava flow thickness (Figs. 5 and 8a). Significant subsidence is also seen near the coast with maximum subsidence of about −0.5 m.

The post-emplacement lava flow deformation rate decays exponentially with time. We selected time series at four sites located near the summit and on the north flank (Fig. 8a) to estimate the exponential decay time constant of the lava flow deformation. We then fit the following decay function to the time series for each site:

$$F(t,\tau) = A \times \left(1 - \exp\left(-\frac{t-t_0}{\tau}\right)\right) \quad (4)$$

in which t_0 is the first post-eruption observation (i.e., 23 January 2008), A is the displacement magnitude, and τ is the

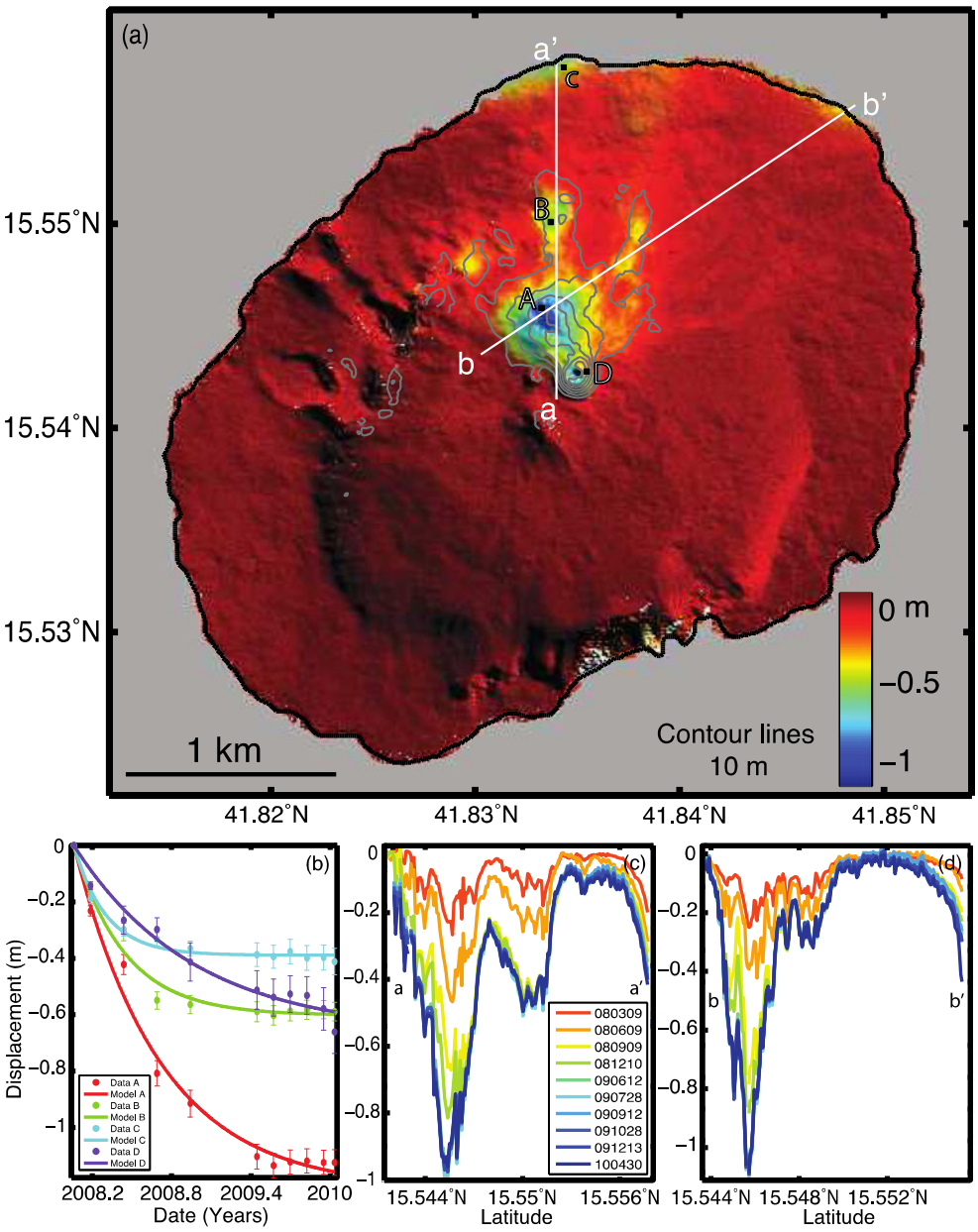

Fig. 8 **a** The post-emplacement displacements of the lava flows in the LOS direction after 23 January 2008 (reference image date). The *cold colors* represent the ground moving away from the satellite. **b** the surface displacement time series (*dots*) for sites *A–D* (locations shown in **a** with their corresponding standard derivation (*bars*) and best-fitting exponential decay curve). **c–d** Surface displacement time series results along profiles *a–a′* and *b–b′*

decay time. The best-fit decay time τ is in the range between 0.24 and 0.9 years, with the decay time at site D larger than at the other test sites. We anticipate that the deformation would stop around 2013 if it followed this function. We found that the eastern flank of the new cone moved by ~−0.13 m between 28 October 2009 and 30 April 2010 (Fig. 8b).

Since the ALOS satellite senses a combination of both horizontal and vertical deformation, the post-emplacement movement of lava flows shown in Fig. 8a can either be due to downslope creep or thermal contraction of the cooling lavas or a combination of the two (Fig. 8c–d). Ebmeier et al. (2012) compiled lava flow subsidence rates observed at several basaltic and andesitic volcanoes, and the maximum lava subsidence rates at Jebel at Tair island are smaller than those observed after the 1997 eruption of Okmok volcano (83 cm/year), which produced a lava flow of 50 m maximum thickness.

Discussion

We have shown that InSAR data together with high-resolution optical satellite images provide valuable information about the 2007–2008 Jebel at Tair eruption. The optical images allow us to map the new ground fissures and the extent of the new lava flow. The InSAR observations provide high-resolution maps of the surface deformation that occurred at the onset of the eruption. These data could also be used to map the evolution, areal extent, and volume of the new lava flows, as well as the post-emplacement lava flow deformation.

Dike intrusions provide information about the state of stress of the medium in which they are emplaced, as their orientation is generally perpendicular to the minimum compressional stress σ_3 (Jónsson 2009). The Jebel at Tair eruptive fissures (and thus the eruption feeder dike) have an average strike of N65°E, meaning that the orientation of the minimum compressional stress at shallow depths was ~N155°E, or roughly parallel to the rift axis of the Red Sea. This may seem like a surprising orientation, given the ongoing active extension of the Red Sea (ArRajehi et al. 2010), but it shows that the stress state of the ~1,400 m high Tair volcanic edifice (258 m above and ~1,200 m below sea level) is isolated from the regional Red Sea stress field. In addition, the optical images exhibit older fissures with other radial trends, with the most recent pre-eruption fissures oriented ~N150°E, or roughly perpendicular to the 2007–2008 fissure. This implies that the stress state of the edifice varies with time and probably changes with each new intrusion. Evidence for time-varying edifice stress fields have been observed at other volcanoes, e.g., at Fernandina volcano, Galápagos, where intrusions alternate between radial flank dikes and circumferential summit dikes (Chadwick et al. 2011; Bagnardi et al. 2013). In addition, Biggs et al. (2013) reported that following a 7–10 km long rift-parallel dike intrusion in northern Tanzania in 2007, a shallower dike with roughly rift-normal trend fed an eruption at the nearby Oldoinyo Lengai volcano.

Volcano-wide deformation caused by pressure changes in subsurface magma reservoirs has been detected (e.g., by InSAR) at many volcanoes in a variety of geological settings. For example at subduction-zone volcanoes in the Aleutians (Lu et al. 2010) and on Kamchatka peninsula (Lundgren and Lu 2006), at hotspot volcanoes in the Galápagos (Jónsson 2009) and Hawaii (Amelung et al. 2007), and at mid-ocean ridge volcanoes in Iceland (Ofeigsson et al. 2011). The absence of pre- and post-eruption deformation at Jebel at Tair, as well as the lack of volcano-wide co-eruption subsidence indicates that the source of the magma may be deep. Assuming a spherical magma chamber (Mogi 1958) underneath Jebel at Tair volcano and a volume change equal to the sum of the estimated subaerial lava flow volume (2.2×10^7 m^3) and the dike volume (5.0×10^6 m^3), the predicted relative LOS displacements, between the summit and the coast, amount to less than 3 cm (~1 Envisat fringe) if the magma chamber depth is larger than 7 km. In other words, if this volume change occurred in a reservoir shallower than 7 km, we should have seen evidence for it in the InSAR data. The lack of a shallow magma reservoir under Jebel at Tair is not unique as deep magma chambers have been detected at other slow-spreading centers (Singh et al. 2006).

Conclusions

No conventional in situ geophysical or geodetic observations are carried out on the remote islands in the Red Sea. Therefore, if not for satellite radar and high-resolution optical images, we might have only known that a SW- and NE-oriented dike fed the 2007–2008 Jebel at Tair eruption. Here, we have used remote sensing data to provide many more details of the Jebel at Tair volcanic activity, which we summarize as follows:

1. Several new fissures were identified in the post-eruption optical images with orientations perpendicular to the Red Sea. Comparison of pre- and post-eruption images shows that a new summit cone formed in the eruption, that the coastline was advanced in places by the new lava, and that the total area of the new lava flow is 5.9±0.1 km^2.
2. The eruption was most vigorous in the beginning, with lava flowing to the coast both in the west and the northeast. Later during the eruption, lava flowed mostly from the summit to the northern flank of the volcano, according to the InSAR decorrelation data. We estimate the bulk lava flow volume to be $2.2\pm1.1\times10^7$ m^3 by taking the height difference between pre- and post-eruption DEMs, which corresponds to an average lava thickness of 3.8 m.

3. The co-eruption deformation data show ~1.2 m of extension across the southwest–northeast striking dike that fed the eruption, which we model with a set of dislocations in an elastic half space. The modeling results suggest that the stress field within the volcano edifice is decoupled from the regional Red Sea extensional stress field. We interpret that the volcano edifice stress field probably changes with each new intrusion, as old fissures on the island exhibit many different radial orientations.
4. The magma source of the 2007–2008 Tair eruption is likely deep (>7 km), as no uplift is found in pre- or post-eruption interferograms and no significant edifice-wide subsidence is seen in the co-eruption data.

Acknowledgments We thank Jamal Sholan (Seismological & Volcanological Observatory of Yemen) for providing information about the Jebel at Tair eruption. We also thank Talfan Barnie (University of Cambridge), Eleonora Rivalta (GFZ Potsdam), Guangcai Feng (KAUST), Teng Wang (KAUST), and Chong Chen (KAUST) for useful discussions, as well as Ahmet Akoglu (KAUST) for help with the GMT software (Wessel and Smith 1998), which was used to prepare Fig. 1a. Comments made by the editor, Matthew R. Patrick, as well as by Juliet Biggs, William W. Chadwick, and one anonymous reviewer helped to improve the manuscript. The European Space Agency (ESA) and the Japanese Aerospace Exploration Agency (JAXA) provided the SAR images used in this study through ESA category-1 project #6703. The TanDEM-X images were provided by the German Aerospace Center (DLR) through project XTI_GEOL3441.

References

Amelung F, Yun SH, Walter TR, Segall P, Kim SW (2007) Stress control of deep rift intrusion at Mauna Loa volcano, Hawaii. Science 316: 1026–1030. doi:10.1126/science.1140035

ArRajehi A, McClusky S, Reilinger R, Daoud M, Alchalbi A, Ergintav S, Gomez F, Sholan J, Bou-Rabee F, Ogubazghi G, Haileab B, Fisseha S, Asfaw L, Mahmoud S, Rayan A, Bendik R, Kogan L (2010) Geodetic constraints on present-day motion of the Arabian Plate: implications for Red Sea and Gulf of Aden rifting. Tectonics 29, TC3011. doi:10.1029/2009TC002482

Bagnardi M, Amelung F, Poland MP (2013) A new model for the growth of basaltic shields based on deformation of Fernandina volcano, Galápagos. Earth Planet Sci Lett 377–378:358–366. doi:10.1016/j.epsl.2013.07.016

Biggs J, Wright T, Lu Z, Parsons B (2007) Multi-interferogram method for measuring interseismic deformation: Denali Fault, Alaska. Geophys J Int 170:1165–1179. doi:10.1111/j.1365-246X.2007.03415.x

Biggs J, Chivers M, Hutchison MC (2013) Surface deformation and stress interactions during the 2007–2010 sequence of earthquake, dyke intrusion and eruption in Northern Tanzania. Geophys J Int 195:16–26. doi:10.1093/gji/ggt226

Bird P (2003) An updated digital model of plate boundaries. Geochem Geophys Geosyst 4:1027. doi:10.1029/2001GC000252

Cervelli P, Murray MH, Segall P, Aoki Y, Kato T (2001) Estimating source parameters from deformation data, with an application to the March 1997 earthquake swarm off the Izu Peninsula, Japan. J Geophys Res 106:11217–11237. doi:10.1029/2000JB900399

Chadwick WW, Jónsson S, Geist DJ, Poland M, Johnson DJ, Batt S, Harpp KS, Ruiz A (2011) The May 2005 eruption of Fernandina volcano, Galapagos: GPS and InSAR observations of a circumferential dike intrusion. Bull Volcanol 73:679–697

Chen CW, Zebker HA (2001) Two-dimensional phase unwrapping with use of statistical models for cost functions in nonlinear optimization. J Opt Soc Am A Opt Image Sci Vis 18:338–351

Clarisse L, Coheur PF, Prata AJ, Hurtmans D, Razavi A, Phulpin T, Hadji-Lazaro J, Clerbaux C (2008) Tracking and quantifying volcanic SO2 with IASI, the September 2007 eruption at Jebel at Tair. Atmos Chem Phys 8:7723–7734. doi:10.5194/acp-8-7723-2008

Dietterich HR, Poland MP, Schmidt DA, Cashman KV, Sherrod DR, Espinosa AT (2012) Tracking lava flow emplacement on the east rift zone of Kīlauea, Hawai'i, with synthetic aperture radar coherence. Geochem Geophys Geosyst 13, Q05001. doi:10.1029/2011GC004016

Ebmeier SK, Biggs J, Mather TA, Wadge G, Amelung F (2010) Steady downslope movement on the western flank of Arenal volcano, Costa Rica. Geochem Geophys Geosyst 11:12. doi:10.1029/2010GC003263

Ebmeier SK, Biggs J, Mather TA, Elliott JR, Wadge G, Amelung F (2012) Measuring large topographic change with InSAR: lava thicknesses, extrusion rate and subsidence rate at Santiaguito volcano, Guatemala. Earth Planet Sci Lett 335–336:216–225. doi:10.1016/j.epsl.2012.04.027

Eckhardt S, Prata A, Seibert P, Stebel K, Stohl A (2008) Estimation of the vertical profile of sulfur dioxide injection into the atmosphere by a volcanic eruption using satellite column measurements and inverse transport modeling. Atmos Chem Phys 8:3761–3805. doi:10.5194/acp-8-3881-2008

Farr TG, Rosen PA, Caro E, Crippen R, Duren R, Hensley S, Kobrick M, Paller M, Rodriguez E, Roth L, Seal D, Shaffer S, Shimada J, Umland J, Werner M, Oskin M, Burbank D, Alsdorf D (2007) The Shuttle Radar Topography Mission. Rev Geophys 45, RG2004. doi:10.1029/2005RG000183

Gass IANG, Mallick DIJ, Cox KG (1973) Volcanic islands of the Red Sea. J Geol Soc 129:275–309. doi:10.1144/gsjgs.129.3.0275

Goldstein RM, Werner CL (1998) Radar interferogram filtering for geophysical applications. Geophys Res Lett 25:4035–4038. doi:10.1029/1998GL900033

International Seismological Centre (2010) Online bulletin. http://www.isc.ac.uk, Internatl. Seis. Cent., Thatcham, UK

Jónsson S (2009) Stress interaction between magma accumulation and trapdoor faulting on Sierra Negra volcano, Galápagos. Tectonophysics 471:36–44. doi:10.1016/j.tecto.2008.08.005

Krieger G, Moreira A, Fiedler H, Hajnsek I, Werner M, Younis M, Zink M (2007) TanDEM-X: a satellite formation for high-resolution SAR interferometry. IEEE Trans Remote Sens Geosci 45:3317–3341. doi:10.1109/TGRS.2007.900693

Lu Z, Fielding E, Patrick MR, Trautwein CM (2003) Estimating lava volume by precision combination of multiple baseline spaceborne and airborne interferometric synthetic aperture radar: the 1997 eruption of Okmok volcano, Alaska. IEEE Trans Remote Sens Geosci 41:1428–1436. doi:10.1109/TGRS.2003.811553

Lu Z, Masterlark T, Dzurisin D (2005) Interferometric synthetic aperture radar study of Okmok volcano, Alaska, 1992–2003: magma supply dynamics and postemplacement lava flow deformation. J Geophys Res: Solid Earth 110:B2. doi:10.1029/2004JB003148

Lu Z, Dzurisin D, Biggs J, Wicks C, McNutt S (2010) Ground surface deformation patterns, magma supply, and magma storage at Okmok volcano, Alaska, from InSAR analysis: 1. Intereruption deformation, 1997–2008. J Geophys Res 115:B00B02. doi:10.1029/2009JB006969

Lundgren P, Lu Z (2006) Inflation model of Uzon caldera, Kamchatka, constrained by satellite radar interferometry observations. Geophys Res Lett 33, L06301. doi:10.1029/2005GL025181

Massonnet D, Feigl KL (1998) Radar interferometry and its application to changes in the Earth's surface. Rev Geophys 36:441–500. doi:10.1029/97RG03139

McClusky S, Reilinger R, Ogubazghi G, Amleson A, Healeb B, Vernant P, Sholan J, Fisseha S, Asfaw L, Bendick R, Kogan L (2010) Kinematics of the southern Red Sea-Afar Triple Junction and implications for plate dynamics. Geophys Res Lett 37, L05301. doi:10.1029/2009GL041127

Mogi K (1958) Relations of the eruptions of various volcanoes and the deformations of the ground surfaces around them. Bull Earthq Res Inst Tokyo Univ 36:99–134

Ofeigsson BG, Hooper A, Sigmundsson F, Sturkell E, Grapenthin R (2011) Deep magma storage at Hekla volcano, Iceland, revealed by InSAR time series analysis. J Geophys Res 116, B05401. doi:10.1029/2010JB007576

Okada Y (1985) Surface deformation due to shear and tensile faults in a half-space. Bull Seismol Soc Am 75:1135–1154

Poland MP (2007) ASAR images a diverse set of deformation patterns at Kilauea volcano, Hawai'i. Proceedings of the ENVISAT Symposium Monteux, Switzerland, 23–27 April 2007, ESA SP-636, 6 pp

Pritchard ME, Simons M, Rosen PA, Hensley S, Webb FH (2002) Co-seismic slip from the 1995 July 30 M_w=8.1 Antofagasta, Chile, earthquake as constrained by InSAR and GPS observations. Geophys J Int 150:362–376. doi:10.1046/j.1365-246X.2002.01661.x

Rowland SK, Harris AJL, Wooster MJ, Amelung F, Garbeil H, Wilson L, Mouginis-Mark PJ (2003) Volumetric characteristics of lava flows from interferometric radar and multispectral satellite data: the 1995 Fernandina and 1998 Cerro Azul eruptions in the western Galapagos. Bull Volcanol 65:311–330. doi:10.1007/s00445-002-0262-x

Shibata T, Kouketsu T (2008) Volcanic clouds from the 2007 eruption of Jebel at Tair (Yemen) detected by ground based and space borne Lidar. SOLA 4:93–96. doi:10.2151/sola.2008-024

Siebert L, Simkin T, Kimberly P (2010) Volcanoes of the world, 3rd edn. Univ of California Press, Berkeley

Singh SC, Crawford WC, Carton H, Seher T, Combier V, Cannat M, Pablo Canales J, Dusunur D, Escartin J, Miguel Miranda J (2006) Discovery of a magma chamber and faults beneath a Mid-Atlantic Ridge hydrothermal field. Nature 442:1029–1032. doi:10.1038/nature05105

Smithsonian Institution (2007) Jebel at Tair. Bulletin of the Global Volcanism Network 32(10)

Smithsonian Institution (2008) Jebel at Tair. Bulletin of the Global Volcanism Network 33(4)

Stevens NF, Wadge G, Williams CA, Morley JG, Muller JP, Murray JB, Upton M (2001) Surface movements of emplaced lava flows measured by synthetic aperture radar interferometry. J Geophys Res 106(B6):11293–11313. doi:10.1029/2000JB900425

Wadge G, Oramas Dorta D, Cole PD (2006) The magma budget of Volcan Arenal, Costa Rica from 1980 to 2004. J Volcanol Geotherm Res 157:60–74. doi:10.1016/j.jvolgeores.2006.03.037

Werner C, Wegmüller U, Strozzi T, Wiesmann A (2000) Gamma SAR and interferometric processing software. In: Proceedings of the ERS-ENVISAT Symposium, Gothenburg, Sweden, pp. 16–20

Wessel P, Smith WHF (1998) New, improved version of generic mapping tools released. Eos Trans AGU 79:579. doi:10.1029/98EO00426

Xu W, Li Z, Ding X, Wang C, Feng G (2012) Application of small baseline subsets D-InSAR technology to estimate the time series land deformation and aquifer storage coefficients of Los Angeles area. Chin J Geophys 55:452–461. doi:10.6038/j.issn.0001-5733.2012.02.009 (in Chinese)